Available online at www.sciencedirect.com

jmr&t Journal of Materials Research and Technology

https://www.journals.elsevier.com/journal-of-materials-research-and-technology

Original Article

Promising applicable heterometallic Al_2O_3/PbO_2 nanoparticles in shielding properties

Atif Mossad Ali[a], *Shams A.M. Issa*[b,c], *Mohamed Rashad Ahmed*[b,d], *Yasser B. Saddeek*[c,e], *Mohd Hafiz Mohd Zaid*[f,*], *Mahmoud Sayed*[a], *Hamoud H. Somaily*[a], *Huseyin Ozan Tekin*[g], *Hj Ab Aziz Sidek*[f], *Khamirul Amin Matori*[f], *Hesham M.H. Zakaly*[d,h,*]

[a] *Physics Department, Faculty of Science, King Khalid University, Abha, 61413, Saudi Arabia*
[b] *Physics Department, Faculty of Science, University of Tabuk, Tabuk city, Saudi Arabia*
[c] *Physics Department, Faculty of Science, Al-Azhar University, Assiut, 71452, Egypt*
[d] *Department of Physics, Faculty of Science, Assiut University, Assiut, 71516, Egypt*
[e] *Department of Physics, College of Science in Zulfi, Majmaah University, Al-Majmaah, 11952, Saudi Arabia*
[f] *Department of Physics, University Putra Malaysia, 43400, Serdang, Selangor, Malaysia*
[g] *Medical Diagnostic Imaging Department, College of Health Sciences, University of Sharjah, Sharjah, 27272, United Arab Emirates*
[h] *Institute of Physics and Technology, Ural Federal University, Ekaterinburg, Russia*

ARTICLE INFO

Article history:
Received 12 August 2020
Accepted 30 September 2020
Available online 8 October 2020

Keywords:
XRD
Al_2O_3
PbO_2
Hetrometal oxides
FLUKA

ABSTRACT

Hetrometal oxides of $(1-x)Al_2O_3/xPbO_2$ (NPs) nanoparticles with different PbO_2 content ($x = 0, 0.3, 0.4, 0.5, 0.6$ and 0.7) have been prepared by irradiation method. The NPs powder has been checked by X-ray diffraction (XRD). XRD measurements affirmed the presence of both pure NPs and nanocomposites of $(1-x)Al_2O_3/xPbO_2$ NPs with different PbO_2 contents. The calculated structural parameters which using the experimental result of XRD charts to give a complete image of these measurements. Moreover, the results using FLUKA code showed that the values attenuation coefficient (μ_m), high effective atomic number (Z_{eff}) and neutron shielding parameters increase as the lead dioxide increase in the Al_2O_3/PbO_2 samples. While the values of half-value layer (HVL) and mean free path (MFP) decrease with increasing PbO_2 content. The investigated shielding features of the chosen Al_2O_3/PbO_2 would be advantageous for exposure control.

1. Introduction

Gamma-ray has been used as worthy instruments in medicinal, cultivation, scientific research. While such applications are very beneficial for human life, undesirable exposures like scattering gamma-rays and cosmic ray are dangerous to human and their environment with different impacts. Exposure to high gamma dose may cause direct hurtful impacts such as radiation sickness and increase the risk of cancer. Thus, how to block gamma radiation that could cause physical harm to a human being [4,5]. The protective material is used to prevent radiation coming from various sources, be it an X-ray room, a laboratory, or a nuclear waste treatment site.

* *Corresponding author.*
E-mails: mhmzaid@upm.edu.my (M.H. Zaid), h.m.zakaly@azhar.edu.eg (H.M. Zakaly).
https://doi.org/10.1016/j.jmrt.2020.09.125

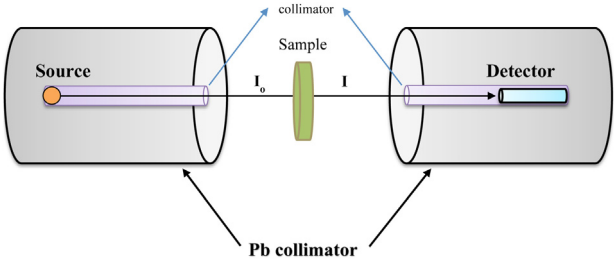

Figure 1 – FLUKA Monte Carlo simulation setup used for mass attenuation coefficients calculations of glasses.

Metal oxides is considered as an exciting goal for researcher because of using them as active components in devices [6,7], organic transformation [8] which give an interesting applications in green science area [9]. Moreover, Al_2O_3 stoichiometry can be used as a catalyst and absorbent [10]. On the other hand, PbO_2 has high chemical stability moreover its promising electrical properties [11,12], achieving the optical transparency with the high electrical conductivity, which reflexes in the optoelectronic industry [13]. It has chemical stability and high micro-hardness [14]. Besides, materials doped with certain heavy metal oxides, such as PbO, have excellent radiation protection properties [15].

So because of their previous interests for metal oxides as well as mixed metal oxides, we study the effect of adding PbO_2 with different content to Al_2O_3 to form $(1-x)Al_2O_3/xPbO_2$ ($x=0$, 30, 40, 50, 60 and 70). Firstly, structural changes have been studied. Then shielding aspects of theses nanoparticle have been investigated.

2. Experiment technique

In this method, 0.2 M $CO(NH_2)_2{\cdot}6H_2O$ was mixed with 0.2 M $Al(NO_3)_2{\cdot}6H_2O$ in a flask, then this mixture was introduced into a 650 W microwave oven for 20 min [1,2]. The final white Al_2O_3 NPs were characterized. The identical procedure has been done for PbO_2 NPs using $Pb(NO_3)_3{\cdot}9H_2O$ as a mother material. Two combinations of metal oxide such as M_1O and M_2O could be mechanical mixing having chemical linkages of M1–O–M2 [16]. For $Al_2O_3/0.3PbO_2$ NPs, 0.7 $Al(NO_3)_2{\cdot}6H_2O$ and 0.3 $PbO(NO_3)_3{\cdot}9H_2O$ were used. The same producers have been done for the rest of concentrations. Shimadzu XD-3A X-ray diffractometer was used for measuring X-ray diffraction (XRD) at angle of 2θ range from 30 to 80, with CuKα radiation source ($\lambda=0.15418$ nm).

FLUKA is a radiation transport code based on Monte Carlo method [17–19]. FLUKA code [20,21] was developed collaboratively by CERN (European Organization for Nuclear Research) and INFN (Italian Institute for Nuclear Physics), can be found elsewhere [17,18] (Fig. 1). In this study, FLUKA Monte Carlo code [22,23] used to investigate the shielding properties of five samples of $(1-x)Al_2O_3/xPbO_2$ nanoparticles (NPs) depending on their densities, with different contents of PbO_2 ($x=0.0$, 0.3, 0.4, 0.5, 0.6 and 0.7) against γ-rays. In the current simulation, The BEAMPOS card used to define the position and direction of the radioactive source which considered as a monoenergetic (0.2 cm dimension), mono-directional beam of photons along

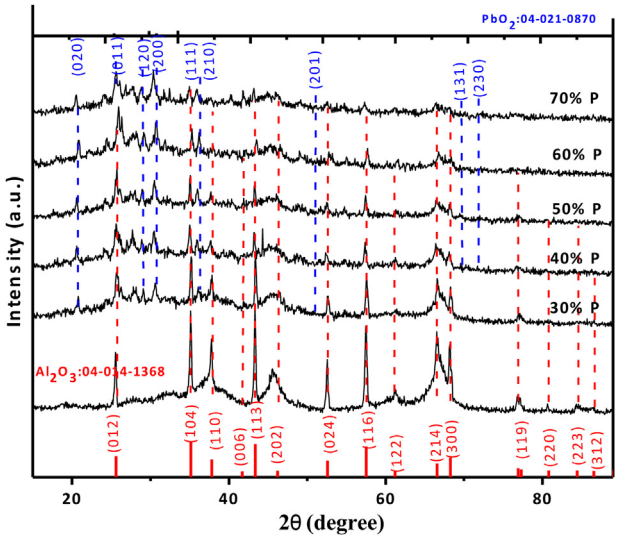

Figure 2 – XRD of $(1-x)Al_2O_3/xPbO_2$ with different PbO_2 NPs content.

plus z-axis with different energies at 1–3 $\times$ 10^3 keV. Then the angular and energy distribution of the source was defined by the BEAM card. Also, the BEAM card defined the type of particle and its energy. For photon transport at low energies, the energy cutoff was set to 10–6 GeV using card EMFCUT. The number of photons reached to detection area detected by a cylindrical 3″ $\times$ 3″ NaI (Tl) scintillation detector [24]. The detector placed inside a collimator made of a 12-cm and 0.2-cm outer and inner diameter with a lead cylinder 13 cm long. The NaI area defined as a track length Fluence estimator by the USRTRACK metrics system. In geometry, each sample placed among the source, and the detector surface indicated in Fig. 1.

MATERIAL card describing the selected composition contains the name of the compound, the weight fraction, the material number, its density, etc. and it is used with the necessary COMPOSITE card to determine the exact composition of the sample

Simulation processes performed between 10^6 and 20^6 primary photons in order to obtain a statistical error of <1%. The fluence of a photon in the detector volume has been assessed with the USRBIN card. The sample was modelled as a cylinder, 4.0 cm diameter, with the various thicknesses from 0.2 to 0.5 cm. Glass samples conducted with the Rectangular Parallelepiped body. RPP characterized by six numbers (minimum and maximum) for X, Y and Z. In this simulation geometry, X (min and max) and Y (min and max) were selected as −5-cm and +5-cm, respectively. Photons passing through the sample were detected in the detector volume.

3. Results and discussion

3.1. *Structural investigations*

XRD was performed for $(1-x)Al_2O_3/xPbO_2$ NPs ($x=0$, 30, 40, 50, 60 and 70) is shown in Fig. 2. XRD pattern of Al_2O_3 NPs shows the peak intensities, as well as positions, are in good agreement with values of Al_2O_3 NPs [Al_2O_3: 04-014-1368]. After

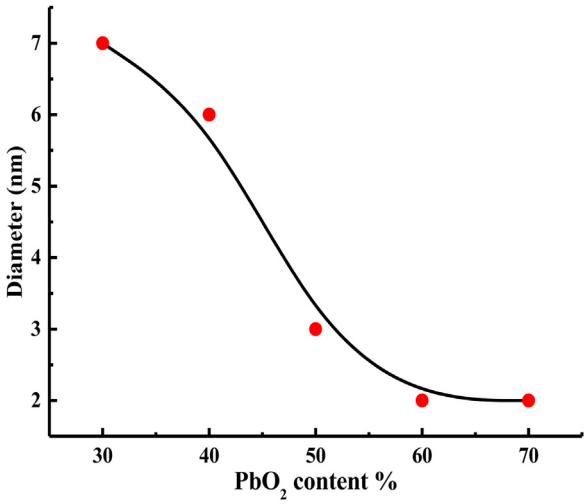

Figure 3 – Size dependence of $(1-x)Al_2O_3/xPbO_2$ on the PbO_2 NPs content.

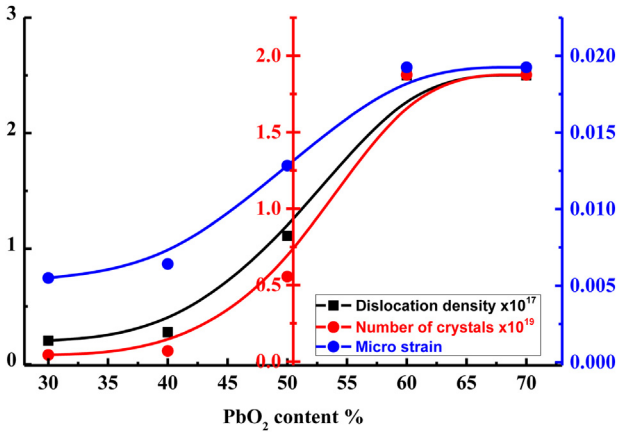

Figure 4 – Dislocation density, number of crystals and dislocation density for $(1-x)Al_2O_3/xPbO_2$ ($x = 0.0$, 0.3, 0.4, 0.5, 0.6 and 0.7) as a function of PbO_2 NPs content.

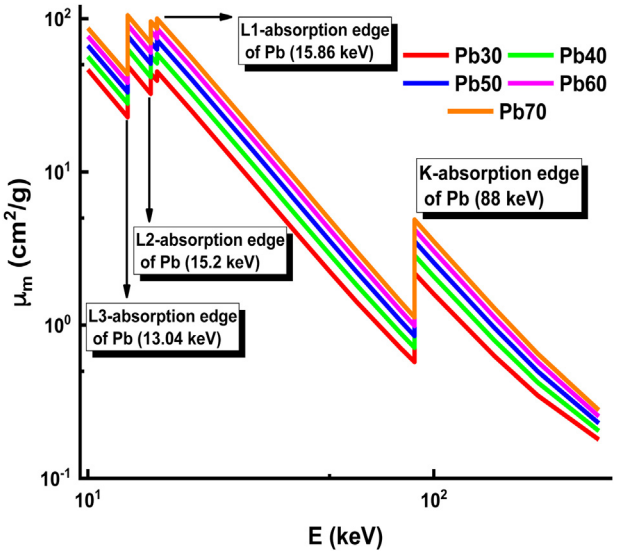

Figure 5 – Mass attenuation coefficient (μ_m) for $(1-x)Al_2O_3/xPbO_2$ ($x = 0.0$, 0.3, 0.4, 0.5, 0.6 and 0.7) as a function of photon energy and PbO_2 content.

adding 0.3 PbO_2 in the Al_2O_3 NPs, the angular positions of the peaks shift slightly, and the peak intensity related to Al_2O_3 NPs starts decreasing. Besides, a peak associated with an impurity (PbO_2) NPs appears [PbO2: 04-021-0870]. As increasing the PbO_2 contents, there is a partial transformation from Al_2O_3 to PbO_2 NPs. The XRD half-width of these peaks was used to calculate the dependence of grain size (D) according to Scherrer's equation [25,26]:

$$D = \frac{K\lambda}{\eta \cos\theta} \tag{1}$$

K: constant, λ: wavelength, θ: Bragg's angle, η: full width at half maximum (FWMH). Fig. 3 shows theses crystalline sizes calculated using Eq. (1). The grain size of as-prepared samples is found to be in the order of nanoscale. The dislocation density, δ is calculated using the following relation [25]:

$$\delta = \frac{1}{L^2} \tag{2}$$

L: thickness.

The microstrain, ε_s is determined by using the relation [27]:

$$\varepsilon_s = \frac{\eta \cos\theta}{4} \tag{3}$$

The crystallites in the unit area, N_c can be calculated by [28]:

$$N_c = \frac{\delta}{L^3} \tag{4}$$

Fig. 4 shows the values of δ, ε_s and N_c for the thin Al_2O_3/PbO_2. It is evident that these values are increasing as the PbO_2 content increases. Thus, the latter results verify that Al_2O_3/PbO_2 crystallinity is enhanced. Substitution and interstitial alloys formation depends on the atomic radii of both components. The substitution alloys are formed because of similar radii of the two metallic components.

On the other hand, an interstitial alloy is allowed to form if these radii are differing [9]. Regarding the ionic radius of Pb2+ and Al2+ is 120 pm and 50 pm, respectively. Therefore, an interstitial alloy of Al_2O_3/PbO_2 is allowed to form.

3.2. *Radiation shielding parameters*

In this study, for Pb30, Pb40, Pb50, Pb60, and Pb70 samples, the related photon attenuation parameters like μ_m, σ_a, HVL, MFP, and Z_{eff} and N_{el} are investigated within 10–300 keV energy range. The μ_m values were evaluated via mixture rule $\mu_m = \sum_i w_i(\mu_m)_i$ obtained by using FLUKA Code. In the low photon energy, a particular photoelectric effect (PEA) interaction process plays an effective role in any material. Here, depending on the sample 'Z' and photon energy (E), PEA $\propto E^{-3.5}Z^{-(4-5)}$ [29–33]. Fig. 5 appears the μ_m transitions, calculated using FLUKA code for Pb30, Pb40, Pb50, Pb60, and Pb70 samples. μ_m exhibits drift

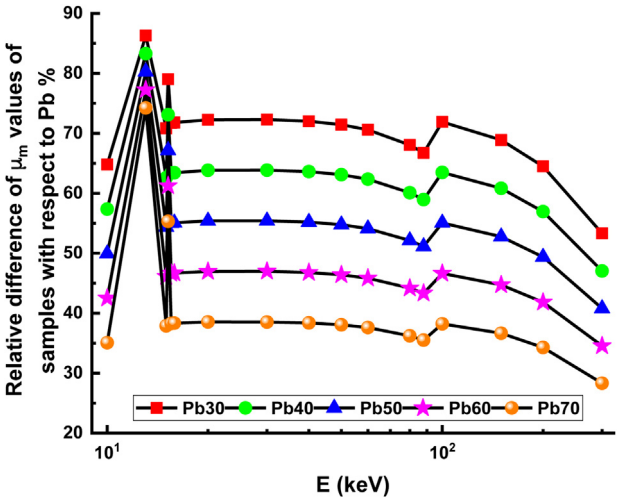

Figure 6 – The relative differences between μ_m values of present samples and μ_m values of Pb metal.

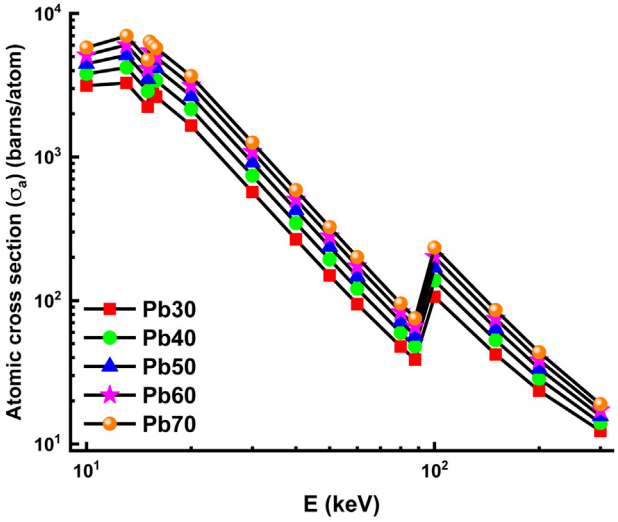

Figure 7 – Atomic cross-section (σ_a) for $(1-x)Al_2O_3/xPbO_2$ (x = 0.0, 0.3, 0.4, 0.5, 0.6 and 0.7) as a function of photon energy and PbO_2 content.

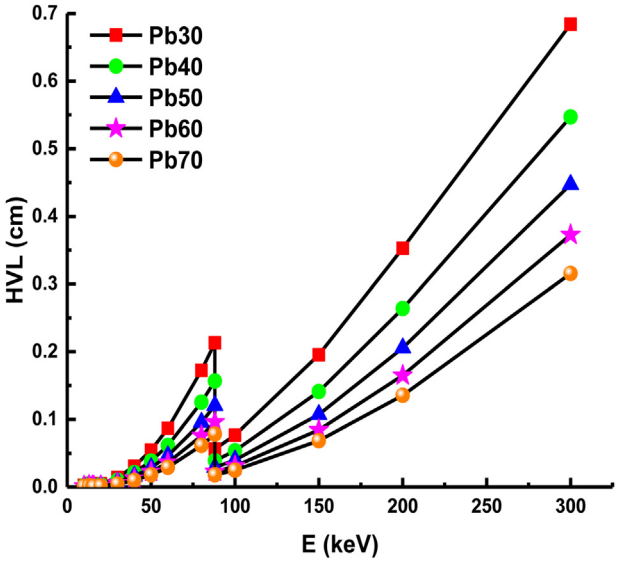

Figure 8 – Half-value layer (HVL) for $(1-x)Al_2O_3/xPbO_2$ (x = 0.0, 0.3, 0.4, 0.5, 0.6 and 0.7) as a function of photon energy and PbO_2 content.

within selected E range for all chosen samples and PbO_2 inclusion instead of Al_2O_3 causes amelioration in μ_m from Pb30 to Pb70 sample as Pb, $Z = 82$ greater than Al, $Z = 13$. Thus, Pb70 sample (contained 70 wt.% PbO_2) has the highest μ_m in all studied samples. 43.25, 52.50, 61.83, 71.13, and 80.72 cm^2/g, for example, are the calculated respective μ_m Pb30, Pb40, Pb50, Pb60, and Pb70 samples at 10 keV.

Moreover, due to PEA domination from 15 to 300 keV, μ_m reduced sharply, though there occurs a quick rise in it at 13.04, 15.2, 15.86 and 88 keV because of Pb element L3, L2, L1 and K-absorption edges, for Pb30, Pb40, Pb50, Pb60, and Pb70 samples. When Pb (82) adding into samples, the interaction between photons and Pb30, Pb40, Pb50, Pb60, and Pb70 will increase. It means that additional energy will be absorbed to drive out an electron from the Pb atom. The electrons could be ejected either through the PEA interaction process [35]. The absorbed radiation through the Pb30, Pb40, Pb50, Pb60, and Pb70 samples is increased, as the interaction of photons with the target atom is increased. Thus, the increment of μ_m values can be predictable. As seen in Fig. 5, the Pb70 sample has the highest value of μ_m. Subsequently, Pb70 sample that contains 70% of PbO_2 has the additional capacity to decrease gamma radiation. The relative differences between the μ_m values for Pb30, Pb40, Pb50, Pb60, and Pb70 samples and the μ_m values for lead are shown in Fig. 6. The chosen metal for compare is lead, which is generally used as a shielding metal in radiation applications. As shown in this figure, the Pb30 sample is 85% bigger μ_m values than lead while Pb70 sample is very close to lead in the chosen energy range. The changes of atomic cross-section (σ_a) values concerning to photon energy are plotted in Fig. 7. The σ_a values of all investigated samples reduce in analogous with the potential of reducing photon–atom interaction. The behaviors of σ_a values with energy and composition are identical to μ_m results obtained for Pb30, Pb40, Pb50, Pb60, and Pb70 samples. Therefore Pb70 and Pb30 sample have the highest and σ_a values in selected photon energy.

The parameters HVL and MFP are very beneficial factors to research the gamma shielding parameters and to evaluate the gamma penetrating strength inside the sample. HVL is the thickness that absorbs the photon intensity by half, and this refers to the ability of photons to penetrate as the energy increases. MFP describes the mean range travelled by a moving photon between two consecutive collisions. HVL and MFP values were estimated for the studied samples via the formulas:

$$\mathrm{HVL} = \frac{Ln(2)}{\mu} \tag{5}$$

$$\mathrm{MFP} = \frac{1}{\mu} \tag{6}$$

where μ is the linear attenuation coefficient. Figs. 8 and 9 show the variation of HVL and MFP values against energy. From fig-

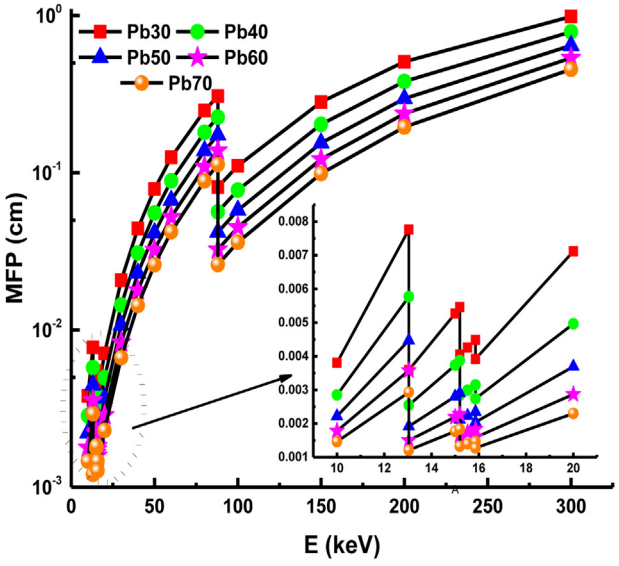

Figure 9 – Mean free path (MFP) for $(1-x)Al_2O_3/xPbO_2$ ($x = 0.0$, 0.3, 0.4, 0.5, 0.6 and 0.7) as a function of photon energy and PbO_2 content.

ures, HVL and MFP values increase as the energy increment. The trend of HVL and MFP with energy could be described identically to the discussion as mentioned earlier of μ_m. In this study, the Pb70 sample has the smallest HVL and MFP values at studied photon energy (10–300 keV) among other investigated samples. As the gamma energy rises to 300 keV, the HVL value becomes 0.33 cm.

The μ_m values could be applied to evaluate the total atomic cross-section (σ_a), total electronic cross-section (σ_e) and effective atomic number (Z_{eff}) via equations [3]:

$$\sigma_a = \frac{\mu_m}{N_A \sum_i^n (w_i/A_i)} \tag{7}$$

$$\sigma_e = \frac{1}{N_A} \sum_i^n \frac{f_i A_i}{Z_i} (\mu_m)_i \tag{8}$$

$$Z_{eff} = \frac{\sigma_a}{\sigma_e} \tag{9}$$

Fig. 10 shows the Z_{eff} values for Pb30, Pb40, Pb50, Pb60, and Pb70 samples. These values are ranged from 14.84 to 45.96. From this figure, it can be observed that the Z_{eff} values raised to two maximums, dependent on PbO_2 content in the Al_2O_3/PbO_2 samples, at 15.20 and 88.00 keV due to L3, L2, L1 and K-absorption edges of Pb element. As shown in Fig. 9, the Z_{eff} values rise as the PbO_2 concentration increment in the Al_2O_3/PbO_2 network. The variations of effective electron density (N_{el}) values versus incident photon energy are presented in Fig. 11. The trend of N_{el} results against photon energy is identical to Z_{eff} behavior. In the selected photon energy, the N_{el} values of investigated samples are Pb30 > Pb40 > Pb50 > Pb60 > Pb70. This may be due to both the weight fraction and atomic mass of the lead constituting the material.

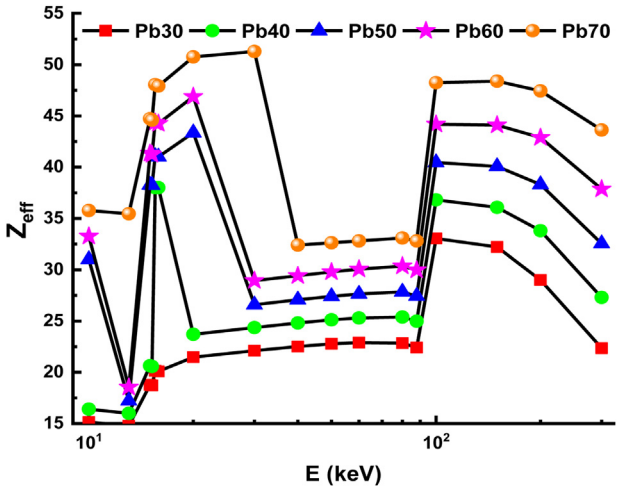

Figure 10 – Effective atomic number (Z_{eff}) for $(1-x)Al_2O_3/xPbO_2$ ($x = 0.0$, 0.3, 0.4, 0.5, 0.6 and 0.7) as a function of photon energy and PbO_2 content.

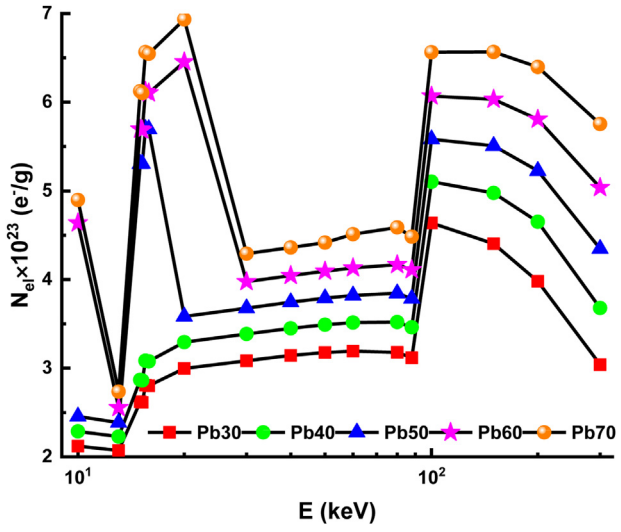

Figure 11 – Effective electron density (Z_{eff}) for $(1-x)Al_2O_3/xPbO_2$ ($x = 0.0$, 0.3, 0.4, 0.5, 0.6 and 0.7) as a function of photon energy and PbO_2 content.

4. Conclusion

$(1-x)Al_2O_3/xPbO_2$ NPs ($x = 0.0$, 0.3, 0.4, 0.5, 0.6 and 0.7) were fabricated and confirmed by experimental XRD results. Size of these NPs was found to be decreasing as the PbO_2 increases. The microstrain, dislocation density and number of crystallites for these NPs were enhanced as a function of PbO_2 contents. μ_m, HVL, MFP, and Z_{eff} radiation shielding properties are calculated to investigate the gamma shielding ability for Pb30, Pb40, Pb50, Pb60, and Pb70 samples. Estimated values show that μ_m, and Z_{effs} values increment as the PbO_2 content increases. Pb70 sample has the smallest HVL and MFP values. Thus, this study refers that Pb70 sample shows distinct protection strength to attenuate the photons.

Declarations of competing interests

None declared.

Acknowledgements

The authors extended their appreciation to the Deanship of Scientific Research at King Khalid University for funding this work through the research group program under grant number R.G.P.2/33/41.

REFERENCES

[1] Darwish AAA, Rashad M, AL-Aoh HA. Methyl orange adsorption comparison on nanoparticles: Isotherm, kinetics, and thermodynamic studies. Dye Pigment 2019;160:563–71, http://dx.doi.org/10.1016/j.dyepig.2018.08.045.
[2] Rashad M, Rüsing M, Berth G, Lischka K, Pawlis A. CuO and Co 3 O 4 Nanoparticles: Synthesis, Characterizations, and Raman Spectroscopy. J Nanomater 2013;2013:1–6, http://dx.doi.org/10.1155/2013/714853.
[3] Limkitjaroenporn P, Kaewkhao J, Limsuwan P, Chewpraditkul W. Physical, optical, structural and gamma-ray shielding properties of lead sodium borate glasses. J Phys Chem Solids 2011;72:245–51, http://dx.doi.org/10.1016/j.jpcs.2011.01.007.
[4] Meulepas JM, Hauptmann M, Lubin JH, Shuryak I, Brenner DJ. Is there unmeasured indication bias in radiation-related cancer risk estimates from studies of computed tomography? Radiat Res 2018;189:128–35.
[5] Mullenders L, Atkinson M, Paretzke H, Sabatier L, Bouffler S. Assessing cancer risks of low-dose radiation. Nat Rev Cancer 2009;9:596–604.
[6] Amigó R, Asenjo J, Krotenko E, Torres F, Tejada J, Brillas E. Electrochemical synthesis of new magnetic mixed oxides of Sr and Fe: composition, magnetic properties, and microstructure. Chem Mater 2000;12:573–9.
[7] Hendi AA, Rashad M. Photo-induced changes in nano-copper oxide for optoelectronic applications. Phys B: Condens Matter 2018:538.
[8] Larsson P-O, Andersson A. Complete oxidation of CO, ethanol, and ethyl acetate over copper oxide supported on titania and ceria modified titania. J Catal 1998;179:72–89.
[9] Rashad M, Amin SA, Ali AM, Hendi AA. Fabrication of p–p type nanocomposite of NiO/Co_3O_4 and CuO/Co_3O_4 with different contents. Mater Res Express 2019;6:0950c9.
[10] Rodríguez JA, Fernández-García M. Synthesis, properties and applications of oxide nanoparticles. New Jersey: Whiley; 2007.
[11] Payne DJ, Egdell RG, Paolicelli G, Offi F, Panaccione G, Lacovig P, et al. Nature of electronic states at the Fermi level of metallic β-PbO_2 revealed by hard x-ray photoem. Phys Rev B 2007;75:153102.
[12] Payne DJ, Egdell RG, Law DSL, Glans P-A, Learmonth T, Smith KE, et al. Experimental and theoretical study of the electronic structures of α-PbO and β-PbO_2. J Mater Chem 2007;17:267–77.
[13] Cordeiro JMM, Azevedo DHM, de Barretto TCM, Sambrano JR. Conducting behavior of crystalline α-PbO_2 as revealed by DFT calculations. Mater Res 2017:21.
[14] Aruna ST, William Grips VK, Rajam KS. Synthesis and characterization of Ni-Al_2O_3 composite coatings containing different forms of alumina. J Appl Electrochem 2010;40:2161–9.
[15] Al-Buriahi MS, Tonguc BT. Study on gamma-ray buildup factors of bismuth borate glasses. Appl Phys A 2019;125:482.
[16] Rashad M, Hamdalla TA, Al Garni SE, Darwish AAA, Seleim SM. Optical and electrical behaviors in NiO/xFe_2O_3 nanoparticles synthesized by microwave irradiation method. Opt Mater (Amst) 2018;75:869–74.
[17] Ferrari A, Sala PR, Fasso A, Ranft J. FLUKA: a multi-particle transport code CERN-2005-10 INFN/TC 05/11, SLAC-R-773; 2005.
[18] Böhlen TT, Cerutti F, Chin MPW, Fassò A, Ferrari A, Ortega PG, et al. The FLUKA code: developments and challenges for high energy and medical applications. Nucl Data Sheets 2014;120:211–4.
[19] Özkalaycı F, Kaçal MR, Agar O, Polat H, Sharma A, Akman F. Lead(II) chloride effects on nuclear shielding capabilities of polymer composites. J Phys Chem Solids 2020;145:109543.
[20] Rashad M, Tekin HO, Zakaly HM, Pyshkina M, Issa SAM, Susoy G. Physical and nuclear shielding properties of newly synthesized magnesium oxide and zinc oxide nanoparticles. Nucl Eng Technol 2020;52:2078–84.
[21] Zakaly HM, Abouhaswa AS, Issa SAM, Mostafa MYA, Pyshkina M, El-Mallawany R. Optical and nuclear radiation shielding properties of zinc borate glasses doped with lanthanum oxide. J Non Cryst Solids 2020;543: 120151.
[22] Elazaka AI, Zakaly HMH, Issa SAM, Rashad M, Tekin HO, Saudi HA, et al. New approach to removal of hazardous Bypass Cement Dust (BCD) from the environment: 20Na_2O–20$BaCl_2$–(60 − x)B_2O_3–(x)BCD glass system and optical, mechanical, structural and nuclear radiation shielding competences. J Hazard Mater 2021;403: 123738.
[23] Abouhaswa AS, Zakaly HMH, Issa SAM, Pyshkina M, El-Mallawany R, Mostafa MYA. Lead borate glasses and synergistic impact of lanthanum oxide additive: optical and nuclear radiation shielding behaviors. J Mater Sci Mater Electron 2020.
[24] Mostafa AMA, Zakaly HMH, Pyshkina M, Issa SAM, Tekin HO, Sidek HAA, et al. Multi-objective optimization strategies for radiation shielding performance of BZBB glasses using Bi_2O_3: a FLUKA Monte Carlo code calculations. J Mater Res Technol 2020;9:12335–45.
[25] Dongol M, El-Denglawey A, Elhady AF, Abuelwafa AA. Structural properties of nano 5, 10, 15, 20-Tetraphenyl-21H,23H-porphine nickel (II) thin films. Curr Appl Phys 2012;12:1334–9.
[26] Moharram AH, Mansour SA, Hussein MA, Rashad M. Direct precipitation and characterization of ZnO nanoparticles. J Nanomater 2014:2014.
[27] Bushroa AR, Rahbari RG, Masjuki HH, Muhamad MR. Approximation of crystallite size and microstrain via XRD line broadening analysis in TiSiN thin films. Vacuum 2012;86:1107–12.
[28] El-Nahass MM, Emam-Ismail M, El-Hagary M. Structural, optical and dispersion energy parameters of nickel oxide nanocrystalline thin films prepared by electron beam deposition technique. J Alloys Compd 2015;646:937–45.
[29] Darwish AAA, Issa SAM, El-Nahass MM. Effect of gamma irradiation on structural, electrical and optical properties of nanostructure thin films of nickel phthalocyanine. Synth Met 2016;215:200–6.
[30] Tekin HO, Kassab LRP, Kilicoglu O, Magalhães ES, Issa SAM, da Silva Mattos GR. Newly developed tellurium oxide glasses for nuclear shielding applications: an extended investigation. J Non Cryst Solids 2019:119763.
[31] Issa SAM, Mostafa AMA, Hanafy TA, Dong M, Xue X. Comparison study of photon attenuation characteristics of Poly vinyl alcohol (PVA) doped with $Pb(NO_3)_2$ by MCNP5 code,

XCOM and experimental results. Prog Nucl Energy 2019;111:15–23.
[32] Issa SAM, Sayyed MI, Kurudirek M. Study of gamma radiation shielding properties of ZnO-TeO_2 glasses. Bull Mater Sci 2017;40:841–57.
[33] Issa SAM, Hamdalla TA, Darwish AAA. Effect of $ErCl_3$ in gamma and neutron parameters for different concentration of $ErCl_3$-SiO_2 (EDFA) for the signal protection from nuclear radiation. J Alloys Compd 2017;698:234–40.
[35] Halimah MK, Azuraida A, Ishak M, Hasnimulyati L. Influence of bismuth oxide on gamma radiation shielding properties of boro-tellurite glass. J Non Cryst Solids 2019;512:140–7.